Earthquake Research Advances 6 (2026) 100391

Contents lists available at ScienceDirect

Earthquake Research Advances

journal homepage: www.keaipublishing.com/en/journals/earthquake-research-advances

Spatiotemporal correlation of multi-depth rock mass deformation and mining-induced subsidence: A case study of the Shagoucha Coal Mine

Dongdong Cao [a], Jun Zhang [a], Ming Li [a], Baoqiang Chen [a], Jia Li [a], Xiaolong Wu [b,*]

[a] China Coal Xi'an Design Engineering Co., Ltd, North Yanta Road No.66, Xi'an, 710054, Shaanxi, China
[b] Xi'an Univerisity of Science and Technology, North Yanta Road No.58, Xi'an, 710054, Shaanxi, China

ARTICLE INFO

Keywords:
Mining-induced subsidence
GNSS
Deep rock mass deformation
Stress adjustment
Cross wavelet transform (XWT) analysis
Time–frequency correlation

ABSTRACT

To address the insufficient understanding of the dynamic coupling between surface subsidence and multi-depth rock mass deformation induced by underground mining, this study focuses on the 520109 working face of the Shagoucha Coal Mine in Shaanxi Province. Most existing subsidence prediction models rely heavily on surface deformation data and often overlook the temporal evolution of deep rock mass responses, limiting their predictive accuracy under complex geological conditions. In this context, we implement a fully integrated GNSS–borehole monitoring system to obtain high-frequency continuous GNSS observations and internal deformation time series at three key depths (14 m, 92 m, and 132 m). To reveal the dynamic correlation between strata deformations and surface subsidence across multiple time scales, cross-wavelet transform (XWT) analysis is applied to quantify both amplitude and phase relationships in the time–frequency domain. The results demonstrate that surface subsidence consistently lags behind deep rock mass deformation, with the deepest monitored stratum (132 m) showing the earliest and largest deformation. The 92 m layer (primary subsidence deformation zone) also displays a leading response, particularly in high-frequency bands, indicating its role in stress redistribution and transmission. In contrast, the shallow 14 m loess layer exhibits a lagging and hydrologically sensitive behavior, responding passively to overlying subsidence. These results highlight the stratified and frequency-dependent nature of deformation evolution, emphasizing the significance of deep rock mass signals as early indicators of subsidence progression. By integrating multi-depth deformation monitoring with time–frequency correlation analysis, this study provides novel insights into the temporal hierarchy of mining-induced subsidence. It provides theoretical support for refining subsidence prediction models and early warning systems. Compared with previous studies that focus primarily on surface or single-depth data, our approach provides a more comprehensive framework for interpreting the spatiotemporal dynamics of stratified deformation processes in mining areas.

1. Introduction

Surface subsidence induced by underground mining is one of the most significant geological hazards faced by mining areas worldwide, directly affecting the ecological environment, infrastructure stability, and mining safety (Ministry of Emergency Management et al., 2022). The deformation of overlying strata in mined-out areas is a key driver of surface subsidence. Rock strata at different depths exhibit distinct deformation characteristics during mining activities, and their cumulative effects ultimately lead to surface subsidence (Zhang et al., 2019, 2024a; Wu, 2021). However, the coupling between surface subsidence and underground rock mass deformation remains unclear, limiting the accuracy of existing subsidence prediction models. Therefore, an in-depth investigation into the correlation between surface subsidence and multi-depth rock mass deformation is crucial for understanding the mechanisms of mining-induced subsidence, improving prediction models, and enhancing safety management in mining areas.

In recent years, numerous studies have been conducted on the spatiotemporal evolution and dynamic mechanisms of mining-induced subsidence. The monitoring techniques for surface subsidence have evolved from traditional leveling surveys and GNSS-RTK measurements to high-frequency continuous GNSS observations, InSAR, and LiDAR-based remote sensing techniques (Wang et al., 2021a; Chen et al., 2020a, 2020b; Lian and Hu, 2017; Yao et al., 2023). Concurrently,

* Corresponding author.
E-mail addresses: xlong_wu@126.com, hawknest@xust.edu.cn (X. Wu).
Peer review under the responsibility of Editorial Board of Earthquake Research Advances.

https://doi.org/10.1016/j.eqrea.2025.100391
Received 17 March 2025; Received in revised form 29 April 2025; Accepted 5 May 2025
2772-4670/© 2025 The Authors. Publishing services by Elsevier B.V. on behalf of KeAi Communications Co. Ltd. This is an open access article under the CC BY-NC-ND license (http://creativecommons.org/licenses/by-nc-nd/4.0/).

various subsidence prediction models have been developed based on the probability integral method (PIM) (Tan et al., 2021; Fan et al., 2018; Wang et al., 2023), finite element method (FEM) (Cao, 2023; Cun and Yao, 2021), and deep learning models (Xiao et al., 2024; Jahanmiri and Noorian-Bidgoli, 2024). However, these methods primarily rely on surface observation data and do not fully account for the deformation evolution of underground rock strata, leading to significant uncertainties in predictions under complex geological conditions.

Moreover, underground rock mass deformation is influenced by multiple factors, including mining activities, geostress variations, and lithological properties. The accuracy of conventional numerical simulations of rock mass deformation heavily depends on initial parameter settings, making it challenging to reflect real deformation processes dynamically (Zhang et al., 2024b). The recent advancements in borehole strain gauges and deep displacement meters have enabled in situ measurements of underground rock mass deformation. To elucidate the relationship between surface subsidence and underground deformation, researchers have employed methods such as time-series correlation analysis and empirical mode decomposition (EMD) to explore their interactions (Diao et al., 2023; Chai et al., 2024; Wang et al., 2024). Although previous studies (Zhang et al., 2021; Guo and Luo, 2022; Wang et al., 2021b) have demonstrated that rock mass deformation varies across different depths, most research has focused on specific depth strata and lacks a comprehensive understanding of the influence of multi-depth rock mass deformation on surface subsidence. Furthermore, these studies are often based on low-frequency or discontinuous observations, making it challenging to capture the time-varying coupling between mining-induced subsidence and multi-layer rock deformation. In response to the limitations of surface-only monitoring in mining subsidence prediction, a growing body of literature has begun to explore the integration of GNSS, InSAR, and wavelet-based signal processing for more robust and high-resolution deformation modeling. For example, Zhang and Cheng (2023) proposed a combined model using wavelet denoising and RBF neural networks to reduce environmental noise and improve the predictive performance of settlement models in deep excavation scenarios (Zhang and Cheng, 2023). Miller and Shirzaei (2015) applied the continuous wavelet transform to separate long-term and periodic deformation signals from InSAR time series in aquifer systems, demonstrating the method's utility in retrieving geomechanical parameters (Miller and Shirzaei, 2015). In the mining context, Wang et al. (2021) integrated GNSS and SBAS-DInSAR observations within a 3D probability integral model inversion framework, enhancing the accuracy of parameter fitting and model prediction (Wang et al., 2021c). More recently, several efforts have coupled SBAS-InSAR with machine learning models, such as robust sequential adjustment and deep learning for near real-time prediction in nonlinear, large-gradient deformation environments (Chen et al., 2024; Yang et al., 2024). These developments highlight a significant trend toward the fusion of multi-source, multi-depth deformation data and advanced computational models to improve prediction accuracy and early warning capabilities in complex mining settings.

To address these gaps, this study investigates the 520109 working face of the Shagoucha Coal Mine in Shaanxi Province. A continuous GNSS observation station was deployed along the strike direction of the working face, and internal deformation meters were installed at different depths beneath the station, including surface loose layers, moderately buried rock layers, and deep confined rock layers. The ground subsidence and dynamic deformation of underground rock strata at multiple depths were synchronously monitored. Furthermore, cross-wavelet transform (XWT) was employed to analyze the time-frequency correlation between mining subsidence and deep deformation, revealing the influence of different depth strata on surface subsidence. This study combines classical methodologies with statistical significance tests and phase vector analysis to propose a theoretically innovative approach, providing new insights into deep engineering deformation monitoring and early warning systems.

2. Study area and geological background

The Shagoucha Coal Mine is located in Xinmin Town, Fugu County, Shaanxi Province, and belongs to the Shenfu mining area. The overall topography of the mine is relatively flat, with the surface primarily covered by Quaternary loess. The research focuses on the 520109 working face, where the coal seam exhibits stable geological occurrence. The primary mining target is the Middle Jurassic Yan'an Formation coal seam, with an average thickness of 3.2 m and a depth of burial ranging from 180 m to 230 m. Fully mechanized top coal caving is employed in this area, which tends to cause significant roof collapse and accelerates the development of subsidence as the working face advances.

The 520109 working face is located in the central part of the coal mine, bordered by the 520110 working face to the east and the 520108 working face to the west. It extends approximately 1 000 m in the north–south direction (strike direction) and about 200 m in the east–west direction (dip direction). The area has a limited history of mining, with subsidence primarily driven by current operations at the 520109 face. As the excavation progresses, a mined-out area forms beneath the surface, and subsidence deformation is expected to continue. To investigate this process, a continuous GNSS observation station was deployed along the strike direction of the working face, and internal deformation meters were installed at three key depths: 14 m, 92 m, and 132 m. These instruments allow for integrated monitoring of deformation patterns in both the surface and underground rock strata. The mine location, GNSS station position, and the general stratigraphic division at the monitoring site are shown in Fig. 1.

The local stratigraphy is representative of typical mining settings in the Ordos Basin and consists mainly of Quaternary loess and Jurassic sedimentary formations. The loess layer is about 20 cm–40 m thick and characterized by a loose structure, high porosity, and sensitivity to hydrological influences. Below this, Jurassic interbedded sandstone and mudstone sequences serve as load-bearing rock masses. Based on geological drilling data and lithological analysis, the selected monitoring depths correspond to the most critical stratigraphic interfaces:

(1) 14 m depth (Near-surface Loose Layer): Located within the Quaternary loess, this layer is highly susceptible to precipitation-induced deformation and typically exhibits delayed mechanical response to mining disturbances.
(2) 92 m depth (Moderately Buried Deformation Zone): Composed of fine sandstone and mudstone interbeds, this layer serves as the primary deformation zone affected by mining-induced stress redistribution.
(3) 132 m depth (Deep Confined Rock Layer): Dominated by thick-bedded sandstone, this mechanically confined stratum plays a dual role in buffering stress and regulating deep rock mass deformation.

The stratigraphic characteristics and deformation responses observed in this area are typical of mining regions in northern Shaanxi and Inner Mongolia. Therefore, the results derived from this case study are expected to be transferable and of practical value to similar geotechnical and mining scenarios in other parts of western China.

3. Data acquisition and processing

3.1. GNSS continuous monitoring data

The GNSS data used in this study were primarily obtained from GNSS displacement monitoring station 01 (Device ID: SJ12DC148698730), which was deployed along the strike direction of the 520109 working face. This station provides a high-frequency three-dimensional displacement time series with a sampling interval of 10 min, allowing for the capture of short-period variations in surface subsidence. All coordinate data were referenced to the China Geodetic Coordinate System 2000

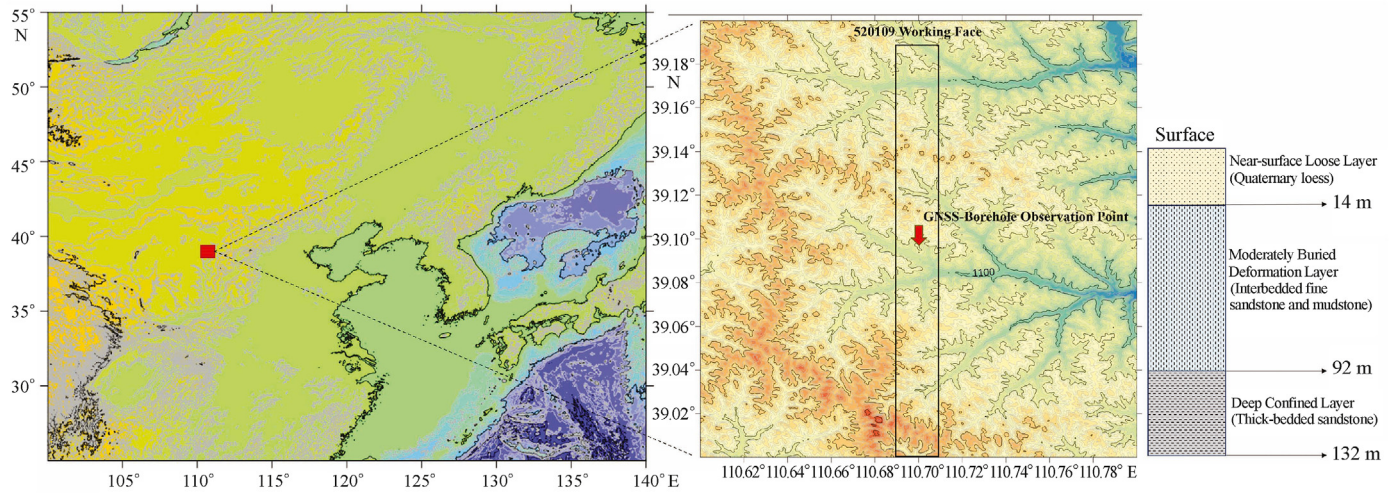

Fig. 1. Location of Shagoucha coal mine, GNSS monitoring station position, and stratigraphic profile at the observation site.

(CGCS2000) and projected onto the Gauss–Krüger plane coordinate system. The vertical subsidence component was derived using a vertical deviation projection method to minimize the influence of horizontal displacement.

A single continuous GNSS station was installed at the center of the 520109 working face to ensure spatial alignment with the borehole-based underground deformation sensors. Fig. 1 illustrates the layout of this station relative to the monitored panel. In addition to the continuous station, a set of conventional GNSS-RTK observation points was deployed, including 27 survey marks along the strike direction and 16 along the dip direction, providing a supplementary spatial framework for characterizing surface displacement patterns.

The GNSS monitoring station is equipped with a high-precision receiver and uses serial communication for data storage and transmission at a baud rate of 9 600. The data are recorded using the S10DZ solution interval format, ensuring consistent accuracy and operational stability. According to established applications in mining deformation monitoring, GNSS systems typically provide positioning accuracy better than ±2 mm for horizontal displacement and within ±10 mm for vertical displacement. The system operates continuously and independently of weather conditions, and offers real-time, automated acquisition, processing, and analysis of high-resolution 3D deformation information—making it particularly suitable for capturing both long-term trends and short-period subsidence events.

To ensure measurement reliability, the GNSS station was configured and operated according to national continuous reference station standards. Its positioning accuracy was validated through internal consistency checks and temporal stability analysis, with repeated baselines confirming horizontal accuracy better than ±2 mm and vertical accuracy within ±10 mm. Although no dedicated field calibration campaign was conducted, the system's long-term stable operation, combined with established data processing protocols and anomaly correction mechanisms, ensures the reliability and repeatability of the recorded displacement sequences.

For data preprocessing, the Hector software package (Bos et al., 2013) was employed to remove outliers and correct observation offsets in the GNSS time series. Hector is specifically designed for the analysis of geodetic station position time series, supporting various colored noise models and robust offset estimation techniques. In this study, raw GNSS coordinates were first transformed from WGS-84 to CGCS2000 and projected using the Gauss–Krüger method to ensure a consistent spatial reference. Hector then automatically identified anomalous points and applied offset corrections caused by instrumental changes or environmental disturbances. Following this, wavelet packet decomposition was employed for denoising, allowing for multi-scale separation and suppression of high-frequency noise, thereby enhancing signal stability and improving the accuracy of subsequent time-series analyses. The long-term trend component was removed using polynomial detrending based on generalized least squares (GLS) estimation under a first-order Gauss–Markov noise model, as provided by Hector, which allows for more accurate isolation of residual deformation signals for wavelet analysis. This trend primarily reflects cumulative mining-induced subsidence, and its removal improves the detection of short-period dynamic deformation responses.

Although no direct comparative experiment was performed in this study to evaluate different denoising algorithms, wavelet packet decomposition was selected based on its established advantages in separating noise-dominated high-frequency components while preserving the underlying trend of geodetic time series. This approach has been widely adopted in previous GNSS and InSAR signal analyses, and provides a balance between time–frequency localization and signal reconstruction accuracy.

3.2. Deep deformation monitoring data

Subsurface deformation monitoring was conducted using an ISAA (Improved Shape Accel Array) system, which features a sampling interval of 10 min. According to manufacturer specifications and field validation studies, the displacement accuracy within a 50 m borehole is better than ±1 mm for high-precision configurations, and within ±3 mm for standard configurations. These sensors are well-suited for high-resolution temporal and spatial analysis of mining-induced rock mass deformation.

The deformation monitoring system consisted of three ISAA sensors (ISAA-14, ISAA-92, and ISAA-132) installed at depths of 14 m, 92 m, and 132 m, respectively. The three monitoring depths were selected based on borehole sampling and lithological analysis conducted at the observation site, which identified these levels as representative of key geological interfaces. Specifically, these depths correspond to the near-surface loess layer, the moderately buried sandstone–mudstone interlayer, and the deep confined sandstone unit. Each sensor records multi-dimensional displacement information, including tilt angles, strain variations, and horizontal deformation, thereby enabling the characterization of deformation propagation under mining-induced stress redistribution. Data are transmitted via serial communication (baud rate: 9600) and stored locally to ensure continuity and reliability.

The raw ISAA time series were processed through the following steps:

(1) Data Cleaning: A mean ± standard deviation method was used to exclude abrupt outliers, while quantile filtering removed statistically anomalous values.

(2) Trend Removal: Long-term drift components were removed using the Hector time series tool to isolate short-period deformation signals.
(3) Data Interpolation: Missing values were filled using cubic spline interpolation to maintain time series continuity.
(4) Denoising Optimization: Wavelet packet threshold denoising was applied to reduce measurement noise and enhance data smoothness for subsequent analysis.

4. Research methodology

4.1. Cross wavelet transform (XWT)

The Cross Wavelet Transform (XWT) combines the Continuous Wavelet Transform (CWT) with cross-spectrum analysis, enabling the exploration of both the amplitude and phase relationships between two non-stationary time series in the time–frequency domain (Torrence and Compo, 1998).

Compared to traditional signal analysis methods such as the Fourier transform or short-time Fourier transform (STFT), XWT provides significant advantages for analyzing geophysical deformation data. While the Fourier transform offers global frequency resolution without time localization, and STFT suffers from fixed window limitations, XWT enables multi-scale, localized analysis of transient features and dynamic correlation.

In this study, XWT is particularly well-suited for characterizing the temporal evolution and phase coherence between surface subsidence and deep rock mass deformation. It allows us to quantify lead–lag relationships across different frequency bands and to investigate how the deformation response propagates among stratified layers under mining-induced stress redistribution. The Morlet wavelet is employed due to its optimal balance between time and frequency resolution, allowing for the effective identification of signal variations across both temporal and spectral dimensions (Foufoula-Georgiou and Kumar, 1995). Its mathematical expression is given by:

$$\psi_0(\eta) = \pi^{-1/4} e^{i\omega_0\eta} e^{-\eta^2/2} \tag{1}$$

Where ω_0 is the dimensionless central frequency, $\eta = s \cdot t$ is the dimensionless time variable, s is the scale parameter, and t is the time variable.

The Morlet wavelet, a complex-valued function, was selected because it enables both amplitude and phase analysis, which is critical for assessing temporal lead–lag behavior between deep deformation and surface displacement. In contrast, real-valued wavelets, such as the Mexican Hat, do not preserve phase information and are thus less suitable for our application. The Morlet wavelet also offers a favorable trade-off between time and frequency resolution, making it suitable for extracting oscillatory behavior in geophysical signals.

In addition to the classical Morlet-based XWT approach adopted here, recent advancements have introduced refined signal decomposition frameworks such as the refined Dual-Scale Filtering (rDSF) method (Yazdanpanah et al., 2022; Mohebi et al., 2021), which also builds upon the Morlet wavelet. These methods integrate dual-scale adaptive filtering with time–frequency decomposition to enhance transient signal components and improve robustness against noise, particularly in vibration and structural health monitoring applications.

Compared to rDSF, which is optimized for single-signal enhancement and feature extraction, the XWT approach used in this study is specifically designed for bivariate analysis, enabling the quantification of time–frequency coherence and phase relationships between two signals. Given that the objective of this study is to examine the spatiotemporal correlation between surface and deep deformation time series, XWT offers a more direct means to assess lead–lag behavior across frequency bands. Nevertheless, the core ideas behind rDSF—especially its enhanced resolution and denoising capabilities—could provide valuable inspiration for the future development of integrated, multi-scale, multi-signal deformation analysis frameworks.

Using the Morlet wavelet as the basis function, the Continuous Wavelet Transform (CWT) of a signal is performed according to Equation (2), converting the target signal into the time-frequency domain.

$$W_x(s,\tau) = \frac{1}{\sqrt{s}} \int_{-\infty}^{\infty} x(t)\psi^*\left(\frac{t-\tau}{s}\right) dt \tag{2}$$

Where s is the scale parameter, τ is the translation parameter, and ψ^* is the complex conjugate of the wavelet function.

For two time series $x(t)$ and $y(t)$, their Continuous Wavelet Transforms (CWT) are performed separately, and the Cross Wavelet Transform (XWT) between them is defined as:

$$W_{xy}(s,\tau) = W_x(s,\tau) \cdot W_y^*(s,\tau) \tag{3}$$

Where $W_y(s, \tau)(s, \tau)$ and $W_y(s, \tau)$ are the CWT coefficients of the two time series, and $W_y^*(s,\tau)$ is the complex conjugate of the wavelet coefficient of $y(t)$. The cross wavelet power $|W_x(s, \tau)|$ reveals the coherence strength between the signals, while the phase difference $\Delta\varphi(s,\tau) = \arg\left(W_{xy}(s,\tau)\right)$ reflects their relative time lag or lead-lag relationship.

Compared to coherence analysis, which captures only frequency-domain correlations, and empirical mode decomposition (EMD), which may suffer from mode mixing and noise sensitivity, the cross wavelet transform (XWT) offers a more robust framework for analyzing non-stationary time series. XWT not only detects localized time-frequency correlation but also quantifies phase relationships between two signals. This makes it particularly suitable for evaluating the dynamic coupling between surface subsidence and multi-depth deformation processes in mining environments.

4.2. Statistical significance test

To assess the reliability of the Cross Wavelet Transform (XWT) results, this study employed a red noise background model to conduct statistical significance testing. Red noise, which characterizes time series with autocorrelation, is particularly suitable for modeling the inherent persistence and low-frequency behavior of geodetic deformation signals.

We assumed that both time series $x(t)$ and $y(t)$ follow a first-order autoregressive process (AR1). The theoretical power spectral density for such a process is given by:

$$P_k = \frac{1-\alpha^2}{\left|1-\alpha e^{-i2\pi k}\right|^2} \tag{4}$$

Where α is the lag-1 autocorrelation coefficient of the AR1 process, and k is the frequency index.

Following the methodology proposed by Torrence and Compo (1998) (Torrence and Compo, 1998), we generated 10,000 Monte Carlo simulations of AR (1) surrogate pairs based on the estimated autocorrelation of the original signals. The cross-wavelet power and phase difference were computed for each simulation, forming a statistical distribution against which the actual XWT results were comparedcross-wavelet power and phase difference were computed for each simulation, forming a statistical distribution against which the actual XWT results were tested.

A two-tailed significance threshold at the 5 % level was applied—only those wavelet power values exceeding the 97.5th percentile or falling below the 2.5th percentile of the red noise distribution were considered statistically significant. This approach ensures that both positive and negative deviations from the null hypothesis of red noise are detected.

The use of the AR (1) model, rather than non-parametric methods such as bootstrapping, is justified by the strong autocorrelation typically observed in deformation time series. The AR(1) framework provides a more physically meaningful approximation of the background noise structure in wavelet-based time-frequency analyses and has been widely validated in geophysical signal processing.

This significance testing framework allows the identification of robust time-frequency regions where the correlation between surface and subsurface deformation exceeds what would be expected from autocorrelated noise alone.

4.3. Algorithm implementation

To ensure comparability between different deformation signals and enhance the numerical stability of the wavelet-based analysis, the original time series were first standardized using Z-score normalization. This process centers each time series to a zero mean and scales it to unit variance, removing the influence of magnitude differences:

$$\begin{cases} x_{\text{norm}}(t) = \dfrac{x(t) - \mu_x}{\sigma_x} \\ y_{\text{norm}}(t) = \dfrac{y(t) - \mu_y}{\sigma_y} \end{cases} \tag{5}$$

Where μ and σ represent the mean and standard deviation of the corresponding non-stationary time series.

To perform the Cross Wavelet Transform (XWT) analysis, the following steps were carried out:

(1) Data Normalization: Standardize the raw time series using Z-score normalization to ensure uniform scale and zero-mean.
(2) Scale Selection: Based on the Nyquist criterion (Grinsted et al., 2004), the minimum scale was defined as $s_min = 2\Delta t$ and the maximum scale as $s_max = N\Delta t/2$, where N is the data length, and Δt is the time interval.
(3) Continuous Wavelet Transform (CWT): Compute the CWT of both normalized time series using the Morlet wavelet to extract their time-frequency representations.
(4) Cross Wavelet Transform (XWT): Multiply the CWT of one signal by the complex conjugate of the other to obtain the cross wavelet power and phase difference.
(5) Significance Testing: Apply the AR (1)-based red noise model with a two-tailed 5 % threshold using Monte Carlo simulations (as detailed in Section 4.2) to identify significant coupling regions.
(6) Cone of Influence (COI) Adjustment: Define the COI to minimize edge effects and restrict interpretation to regions outside this boundary.
(7) Phase Vector Interpretation: Analyze the direction of arrows in the XWT output to determine lead-lag relationships and correlation polarity (see Section 5.2).

To further enhance clarity, an algorithmic flowchart summarizing the above steps is provided in Fig. 2.

4.4. Change-point detection based on the PELT algorithm

To segment the cumulative surface subsidence time series into representative deformation phases, we adopted the Pruned Exact Linear Time (PELT) algorithm, which is well-suited for identifying multiple change-points in large time series with linear computational complexity (Killick et al., 2012). The cost function used was the residual sum of squares (RSS), and a penalty parameter β was introduced to control the trade-off between overfitting and sensitivity.

The implementation was conducted using the ruptures package in Python. The GNSS-derived cumulative subsidence sequence was input as a one-dimensional array, and the PELT algorithm with CostRuptures ("l2") was applied. The penalty value was empirically determined through iterative testing, with β set to $3 \times \log(n)$, where n is the sequence length.

To enhance the robustness of the results, a post-processing filter was applied: only change-points associated with cumulative displacement jumps greater than 10 mm, and persistent over at least two sampling intervals (20 min). This procedure allowed us to divide the deformation process into three stages—stable, initial, and accelerated deformation—which are used in Section 5.1 and annotated in Fig. 2.

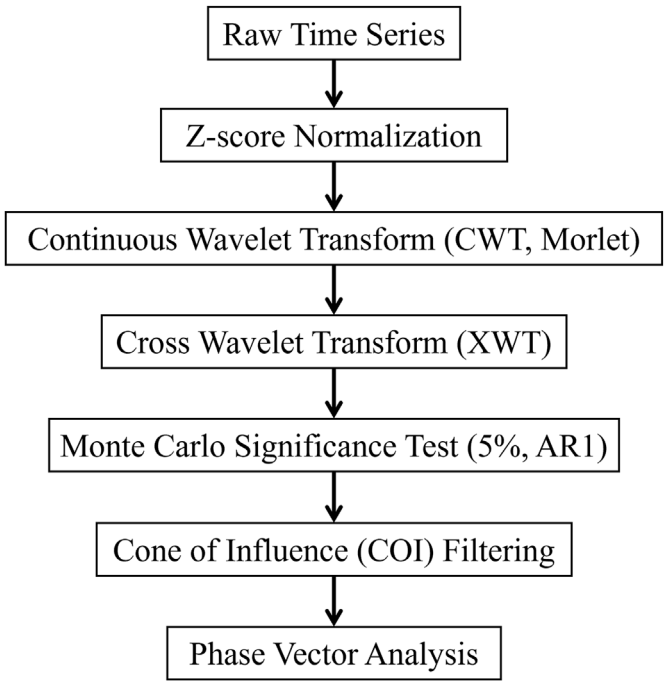

Fig. 2. Workflow of cross-wavelet transform (XWT) analysis for multi-depth deformation correlation.

To reduce false positives caused by minor oscillations or measurement noise, a post-filtering step was applied to the PELT results. Change-points were retained only if they were associated with cumulative displacement increases exceeding 10 mm and lasting for at least two consecutive sampling intervals. This conservative criterion ensured that only major structural changes were emphasized in the visual outputs.

5. Results

5.1. Time series characteristics

It is important to note that the internal deformation meters deployed in this study are configured to capture only horizontal displacements (in the x- and y-directions), while vertical displacements at depth could not be obtained due to technical limitations in the borehole system. Given that the primary objective of this study is to investigate the spatiotemporal relationship between deep rock mass deformation and surface subsidence, comparing horizontal deformation at depth with vertical surface displacement is both reasonable and meaningful. Surface subsidence over the mining panel is a central focus in mining geomechanics and subsidence-related research, as it directly affects infrastructure safety and environmental stability. By analyzing the correlation between these different components, we aim to better understand how subsurface lateral stress redistribution and deformation contribute to vertical surface settlement.

As shown in Fig. 3, the cumulative subsidence deformation time series observed by the GNSS monitoring station is presented. Based on the Pruned Exact Linear Time (PELT) change-point detection algorithm, the subsidence deformation at the station location can be divided into three evolutionary stages:

(1) Stable Stage (August 12 – October 5): During this period, the working face had not yet advanced to the monitoring station location. The roof remained supported by intact rock strata, and

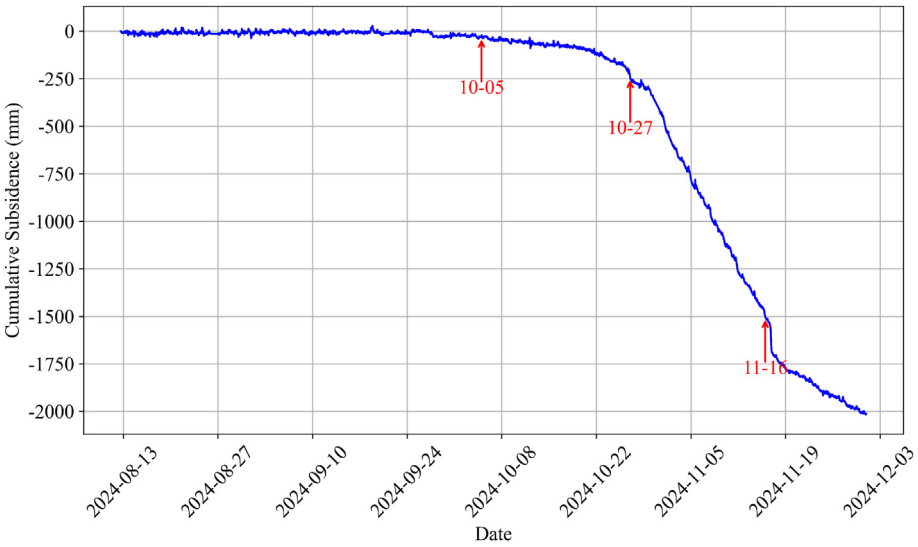

Fig. 3. Cumulative subsidence displacement time series from GNSS continuous observations.

the cumulative subsidence displacement fluctuated around zero, with a total displacement of approximately 22 mm. The overburden in this stage retained its original stress equilibrium, with high integrity and limited stress disturbance. The presence of effective pre-mining support pressure in front of the working face likely helped maintain structural stability.

(2) Initial Deformation Stage (October 5–October 27): As the working face approached the monitoring point, the curvature of the cumulative displacement curve increased, indicating the onset of surface deformation. By the end of this stage, cumulative subsidence reached approximately 256 mm.

(3) Accelerated Deformation Stage (October 27–November 16): Significant surface subsidence occurred during this period. On November 16, 2024, a roof failure was observed in the deep overlying strata, resulting in a sudden increase in displacement. The total cumulative subsidence by this point reached approximately 1 534 mm.

Fig. 4(a) and (b) illustrate the cumulative deformation trends at a depth of 14 m. In the initial stage of the time series, the x-direction (strike direction) displacement shows a negative trend, indicating southward contraction of the rock mass. Over time, the displacement shifts to a positive direction by November 16, signifying northward expansion of the rock layer. The *y*-direction (dip direction) displacement initially exhibits a negative growth trend, suggesting westward compression of the rock mass. However, after November 2, the displacement curve reverses to a positive growth trend, indicating eastward expansion. The 14 m depth rock mass undergoes a transition from initial compression to later expansion, suggesting that localized stress release and layer expansion may have occurred during the mining process.

Fig. 4(c) presents the cumulative deformation in the *x*-direction at a depth of 92 m. Initially, the deformation trend is negative, indicating southward contraction of the rock mass. Later, the displacement turns positive, indicating northward expansion, a trend similar to that observed at 14 m depth. Fig. 4(d) shows the *y*-direction (dip direction) deformation at 92 m, where the initial negative displacement indicates westward compression, which later accelerates. By November 16, the displacement increases further in the negative direction, indicating continued westward compression. The *x*- and *y*-direction (dip direction) deformations at 92 m depth exhibit a typical compression-to-expansion transition, while the *y*-direction (dip direction) acceleration in compression suggests that this layer experienced significant stress concentration and localized deformation.

Fig. 4(e) and (f) depict the cumulative deformation curves at 132 m depth in the x- and y-directions, respectively. In the x-direction, the initial negative displacement represents southward contraction, which later transitions to a positive displacement, indicating northward movement following stress release. Compared to 92 m depth, the x-direction (strike direction) changes at 132 m are smoother, implying that deformation in the deep confined rock layer occurs at a slower rate. In the y-direction (dip direction), an initial negative growth trend signifies westward contraction, which continues until November 16, when the displacement increases further in the negative direction, indicating continued westward compression. Both the x- and y-direction (dip direction) deformations at 132 m depth exhibit a compression-to-expansion transition, albeit at a slower rate, suggesting that the deformation behavior of the deep confined layer differs from that of the upper layers and is likely influenced by wider stress redistribution effects.

In general, at 14 m depth, the deformation process is characterized by a clear transition from compression to expansion, particularly in the y-direction. Given that this depth corresponds to the loess layer, its loose structure is highly susceptible to hydrological changes (e.g., precipitation or groundwater fluctuations), which may cause rock mass expansion or contraction. Additionally, mining activities may induce localized stress release, leading to layer expansion, especially evident in the y-direction (dip direction) fluctuations.

Compared to 14 m depth, the deformation at 92 m depth exhibits accelerated compression characteristics, particularly in the y-direction (dip direction). This suggests that this layer may be located within a high-stress zone, where stress concentration effects induced by mining activities are more pronounced. The interbedded fine sandstone and mudstone at this depth results in a complex stress response, leading to more significant compression-expansion transitions.

At 132 m depth, the deformation curves show that the magnitude of deformation is significantly smaller than at 92 m depth, especially in the x-direction (strike direction), where the intensity of deformation is notably lower. This may be attributed to the predominance of thick-bedded sandstone at this depth, which plays a key role in controlling subsidence and deformation, leading to a slower deformation response.

By comparing Figs. 3 and 4, it can be observed that abnormal deformation trends at the monitoring station first appeared in the x-direction at a depth of 132 m. The deformation curve exhibited a significant acceleration in southward deformation on September 19, 2024. Correspondingly, in the y-direction (dip direction), the stable eastward deformation trend began to weaken after September 16, 2024, eventually reaching a quasi-static state. Subsequently, abnormal cumulative deformation trends were

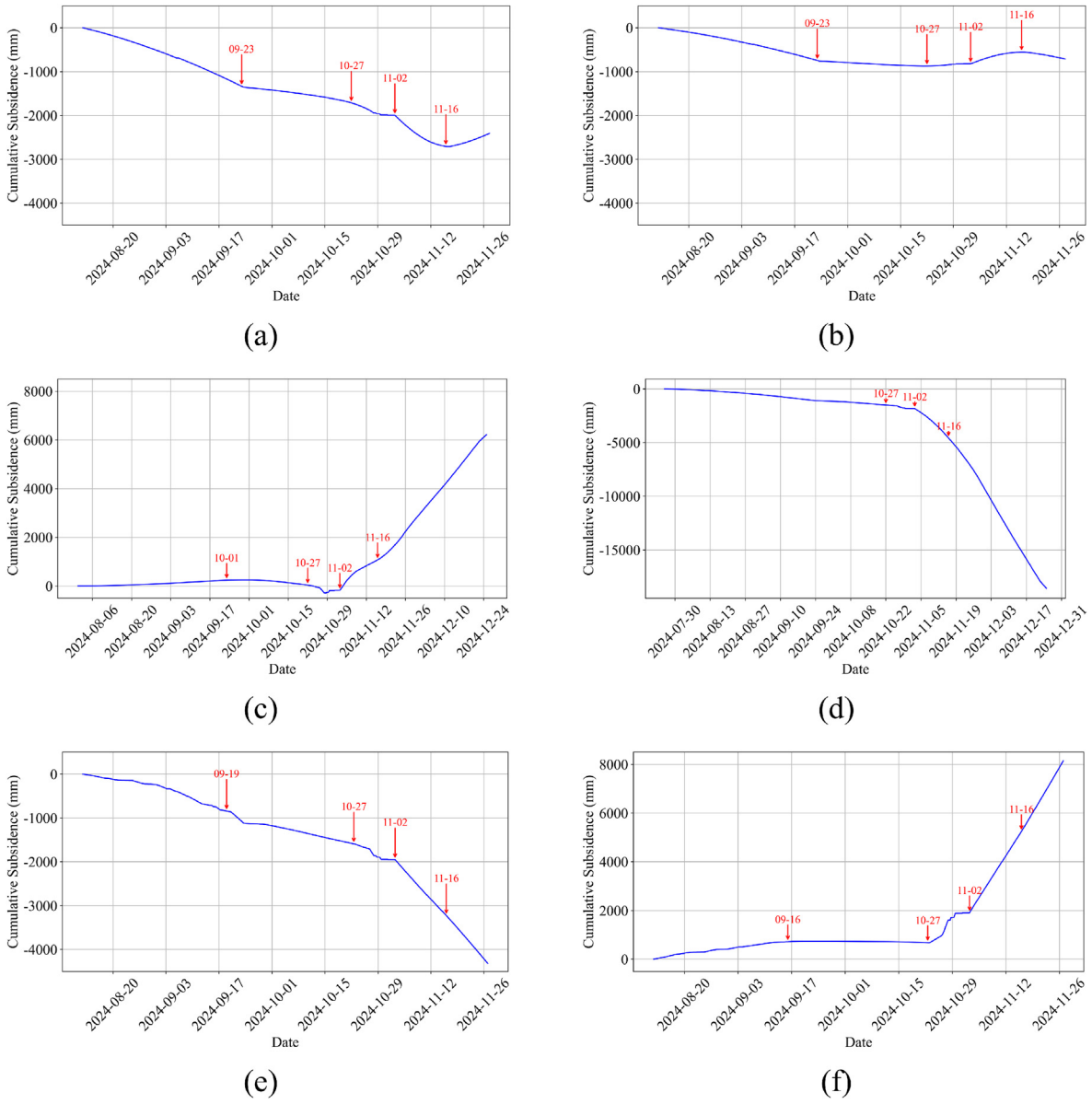

Fig. 4. Cumulative Horizontal Deformation Time Series at Different Depths. (a) Cumulative deformation time series in the x-direction (strike direction) at 14 m depth; (b) Cumulative deformation time series in the y-direction (dip direction) at 14 m depth; (c) Cumulative deformation time series in the x-direction (strike direction)at 92 m depth; (d) Cumulative deformation time series in the y-direction (dip direction) at 92 m depth; (e) Cumulative deformation time series in the x-direction (strike direction) at 132 m depth; (f) Cumulative deformation time series in the y-direction (dip direction) at 132 m depth. Red points indicate PELT-detected change-points filtered by displacement magnitude (>10 mm) and persistence (>20 min). Visually noticeable but short-lived or minor fluctuations (e.g., on 22 Sep and 29 Oct) were not retained under this selection criterion.

detected at 14 m depth on September 23 and at 92 m depth on October 1, respectively. Meanwhile, the initial deformation stage observed by surface GNSS monitoring was first recorded on October 5, which was later than the deformations observed at all deeper layers. Notably, during the period from October 27 to November 2, synchronous and consistent anomalous deformation fluctuations occurred in all deep layers in the horizontal direction.

5.2. *Cross wavelet transform results analysis*

5.2.1. *Correlation between 14 m Depth Deformation and Surface Subsidence*

In the XWT phase plots, arrows represent the relative phase relationship between the deep deformation signal and the surface subsidence time series derived from GNSS. Specifically, arrows pointing to the right indicate that the two signals vary in phase, while arrows pointing to the left denote anti-phase behavior. Arrows pointing upward suggest that the deep deformation signal leads the surface subsidence, whereas arrows pointing downward indicate that deep deformation lags behind the GNSS-derived response. These directional indicators provide intuitive insight into the timing and correlation polarity between subsurface and surface deformation across different frequency bands. This vector interpretation enables the identification of temporal causality and coordination in subsidence development, especially in stratified mining environments.

As shown in Fig. 5(a), the statistically significant correlation between surface subsidence and the x-direction horizontal deformation at 14 m depth is mainly concentrated between September 17 and November 13, 2024, encompassing the stable, initial, and accelerated deformation stages.

In the frequency domain, strong correlation is concentrated in the

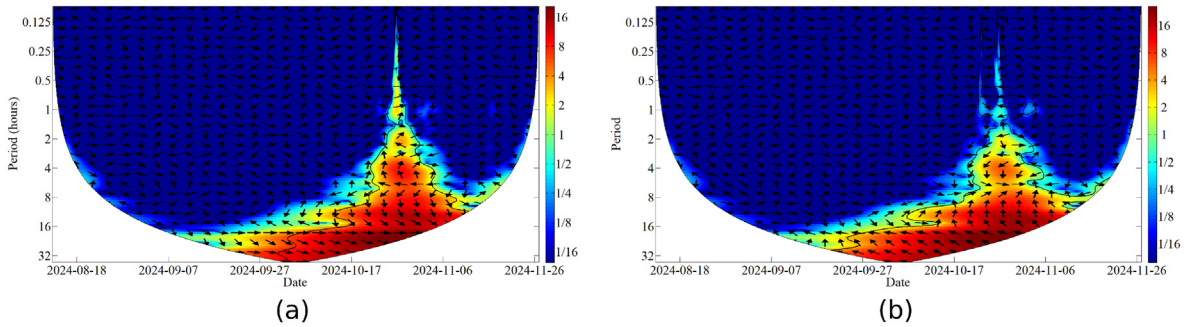

Fig. 5. Cross Wavelet Transform Results Between 14 m Depth Deformation and Surface Subsidence (Phase arrows: right = in-phase; left = anti-phase; up = deep deformation leads; down = deep deformation lags.).

low-frequency band (>12 h), suggesting that deep deformation and surface subsidence share similar long-term variation patterns. In the 3–6 h frequency range, localized correlation peaks are observed between October 24 and November 6, aligning with the transition from stable to accelerated surface subsidence.

During this phase, phase vectors are predominantly oriented upward, indicating that x-direction deformation at 14 m depth temporally leads surface subsidence and may serve as a precursor to near-surface movement. In the low-frequency range, phase vectors also exhibit a strong in-phase orientation, suggesting synchronized long-term deformation behavior between this layer and the surface. Fig. 5(b) illustrates the time-frequency correlation between the *y*-direction displacement at 14 m depth and surface subsidence. Compared to Fig. 5(a), the significant correlation regions are broadly similar, but the phase vector orientations differ notably. In the low-frequency significant correlation region, phase vectors are generally oriented to the left, indicating that y-direction deformation at 14 m depth is negatively correlated with surface subsidence. This suggests that as surface subsidence intensifies, horizontal displacement in the *y*-direction at this depth tends to exhibit an opposite trend. In the 3–6 hr localized correlation band, phase vectors point downward, signifying that *y*-direction deformation lags behind surface displacement at this frequency range, highlighting a passive response of the shallow layer to rapid surface changes. The observed temporal lag between deformation at depth and surface subsidence may result from differences in mechanical response across stratigraphic layers. Variations in lithology, stiffness, or fracture density may influence the rate at which stress is redistributed and deformation is transmitted upward.

5.2.2. Correlation between 92 m Depth Deformation and Surface Subsidence

In the high-frequency range (3–8 hours), phase vectors predominantly point upward, indicating that x-direction deformation at a 92-m depth leads to surface subsidence. This suggests a possible precursor effect, where deep deformation may initiate short-period surface movement. The 92 m layer is composed of interbedded fine sandstone and mudstone, whose contrasting mechanical properties contribute to anisotropic stress responses. Mudstone layers tend to compress more easily, while sandstone offers greater stiffness and confinement, leading to localized stress concentration and dynamic shear zones, which may explain the observed frequency-dependent deformation patterns.

In the very high-frequency range (<1 hr), the significant correlation is limited to October 26–30, 2024, coinciding with the transition from initial to accelerated surface deformation. However, within this time-frequency range, the phase vectors show low consistency, indicating a more complex or less stable relationship. These irregular patterns may be associated with transient mining disturbances or localized stress redistributions during critical subsidence stages.

As shown in Fig. 6(b), the time-frequency correlation between the *y*-direction displacement at 92 m depth and surface subsidence displays a similar pattern to that of the *x*-direction, with some differences in phase orientation. In the low-frequency range (>8 hr), statistically significant regions are relatively stable, and the phase vectors generally point downward-right, indicating a positive correlation. This suggests that in long-term trends, deformation in the y-direction at this depth is synchronized with surface subsidence, possibly due to the gradual redistribution of stress. In the high-frequency band (2–4 hr), *y*-direction deformation leads to surface displacement, resembling the *x*-direction behavior. This may indicate that short-term deformation at this depth contributes to the onset of surface subsidence.

This phenomenon may be influenced by multiple factors, such as periodic loading induced by the advancement of the working face, which causes fluctuations in *y*-direction deformation and, through stress transfer, affects the surface subsidence process. Compared to the *x*-direction, the statistically significant region for *y*-direction deformation is slightly narrower and more localized in the time-frequency domain, which may be related to structural anisotropy or stress concentration along the dip direction.

5.2.3. Correlation between 132 m Depth Deformation and Surface Subsidence

As shown in Fig. 7(a), high-power regions of statistically significant

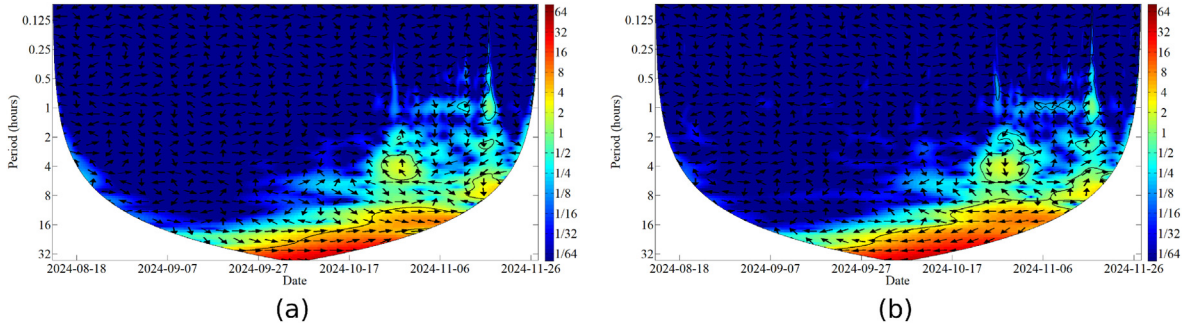

Fig. 6. Cross Wavelet Transform Results Between 92 m Depth Deformation and Surface Subsidence (Phase arrows: right = in-phase; left = anti-phase; up = deep deformation leads; down = deep deformation lags.).

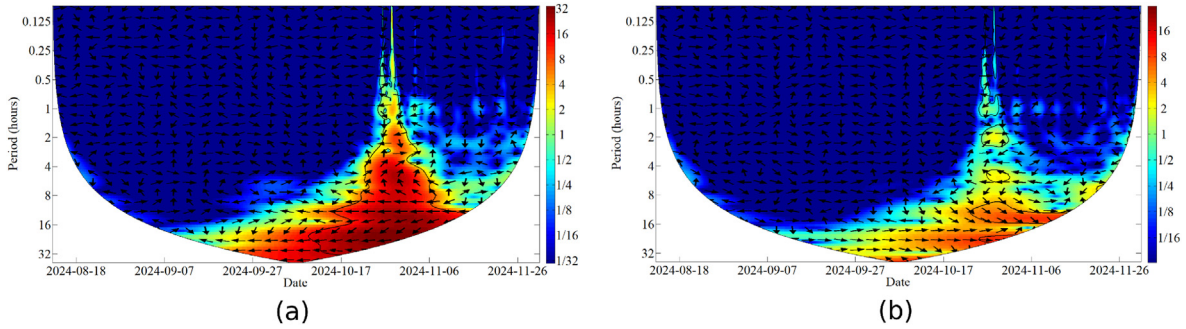

Fig. 7. Cross Wavelet Transform Results Between 132 m Depth Deformation and Surface Subsidence (Phase arrows: right = in-phase; left = anti-phase; up = deep deformation leads; down = deep deformation lags.).

correlation from the cross wavelet transform are concentrated between September 30 and November 11, 2024. This time window begins earlier than the corresponding deformation at a depth of 92 m and nearly spans the entire initiation and acceleration phases of surface subsidence. These results indicate that x-direction deformation at 132 m depth is strongly associated with surface movement during mining-induced subsidence. The 132 m depth is predominantly composed of thick-bedded sandstone, a lithology known for its high stiffness and low compressibility. These characteristics enable the layer to act as both a stress transmission path and a buffering zone, resulting in early activation of deformation under mining-induced stress perturbations.

In the frequency domain, the correlation between surface subsidence and *x*-direction deformation at 132 m depth exhibits distinct segmentation:

(1) Low-Frequency Region (>16 hr): Phase vectors predominantly point to the right with a slight downward inclination, indicating a negative correlation and a minor lag. This suggests that long-term deep deformation at this depth evolves in an opposite direction to surface subsidence, possibly reflecting delayed structural adjustment under sustained stress.
(2) Mid-Frequency Region (6–16 hr): Phase vectors mostly point downward, suggesting that deformation at this depth lags behind surface subsidence. This may indicate a passive response where deep deformation is driven by stress redistribution following surface movement during mining advancement.
(3) High-Frequency Region (<6 hr): Phase vectors tend to shift upward, though with weak directional consistency, implying a limited leading behavior of deep deformation relative to surface subsidence. The significant region in this frequency band is narrow and concentrated around October 27–31, 2024, corresponding to the transition from initial to accelerated surface deformation.

As shown in Fig. 7(b), the statistically significant region for *y*-direction deformation at 132 m depth exhibits a similar overall distribution to that of *x*-direction deformation, suggesting a potentially common response to mining-induced disturbances such as stress redistribution or localized fracturing. However, the significant region for *y*-direction deformation is smaller and more scattered, indicating lower spatial coherence compared to the *x*-direction component. These differences may stem from bedding structure or microfracture development that limits coherent strain propagation in the dip direction.

(1) Low-Frequency Region (>16 hr): Phase vectors are oriented slightly leftward, indicating a negative correlation between *y*-direction deformation and surface subsidence. This may reflect an inverse feedback response at longer timescales.
(2) Mid-Frequency Region (6–16 hr): Phase vectors predominantly point downward with localized divergence, suggesting that deformation in the *y*-direction lags behind surface displacement and acts primarily as a passive response to mining-induced stress changes.
(3) High-Frequency Region (<6 hr): Phase vectors are mostly upward-facing, indicating a limited leading behavior of *y*-direction deformation relative to surface subsidence. Compared to the *x*-direction component, this response appears weaker and may be associated with minor short-term adjustments under localized shear activity.

To facilitate a comparative overview, the cumulative displacement values observed at each depth are summarized in Table 1. Table 2 Summary of phase characteristics and correlation patterns between surface subsidence and deep deformation at different depths across frequency bands.

6. Discussion

6.1. Correlation between surface subsidence and deformation at different depths

Although the displacement components differ in direction, their comparison is essential because the central focus of this study is surface subsidence. We aim to understand how horizontal deformation occurring at depth, which may indicate stress redistribution or shear failure, correlates with and potentially drives vertical ground settlement. To explore this relationship, we performed a joint analysis of vertical GNSS-derived surface subsidence and horizontal borehole deformation across three depths using cross wavelet transform techniques.

This study investigates the correlation between surface subsidence and subsurface deformation at different depths (14 m, 92 m, and 132 m) based on GNSS surface subsidence observations and internal deformation monitoring data, combined with cross wavelet transform analysis. The results indicate that deformation at all depth levels occurs earlier than surface subsidence and exhibits different response patterns, reflecting the key role of rock mass structure characteristics and stress adjustment mechanisms in subsidence evolution.

From the time series evolution trends, the initial deformation stage of surface subsidence (October 5) is significantly delayed compared to the anomalous deformation events observed at different depths. Specifically, *x*-direction (strike direction) deformation at 132 m depth underwent a sudden change on September 19, followed by trend anomalies at 92 m

Table 1
The cumulative displacement values observed at each depth.

Depth(m)	*y*-direction Deformation (mm)	*x*-direction Deformation(mm)
14	-2 407	711
92	6 241	−1 8470
132	-4 319	8 140

Table 2
Summary of phase characteristics and correlation patterns.

Depth(m)	Low Frequency (>12–16 h)	Medium–High Frequency (2–8 h)
14	*x*: In-phase; long-term synchronization *y*: Negative correlation with slight lag; inverse trend	*x*: Leads surface subsidence; precursor behavior *y*: Lags surface subsidence; passive response
92	*x*: Negative correlation; phase leads surface subsidence *y*: In-phase; spatially localized correlation	*x*: Leads surface subsidence; strong triggering potential *y*: Leads slightly; supports short-term propagation
132	*x*: Negative correlation; leads subsidence *y*: Negative correlation; lower coherence	*x*: Leads surface subsidence; moderate consistency *y*: Weaker response; minor short-term effect

depth on September 23 and 14 m depth on October 1. This suggests that deep rock mass deformation occurs before surface subsidence becomes apparent and plays a driving role in the subsequent stress transfer process leading to surface movement. Additionally, during October 27 to November 2, synchronous anomalous fluctuations in horizontal deformation across all depth levels indicate that subsidence evolution entered a coordinated deformation phase.

Cross-wavelet transform analysis further reveals the time-frequency correlation between different depth layers and surface subsidence:

(1) Deformation at a 14-m depth primarily exhibits strong in-phase variations with surface subsidence in the low-frequency range (periods greater than 12 hours), suggesting a strong coupling between the deformation of this layer and surface subsidence. However, in the high-frequency range (3–6 h), y-direction (dip direction) deformation lags behind surface subsidence, likely due to the loose structure of the loess layer at 14 m depth.
(2) Deformation at 92 m depth displays a negative correlation with surface subsidence in the low-frequency range (8–32 h) for x-direction (strike direction) displacement, while in the high-frequency range (3–8 h), deep deformation precedes surface subsidence. This indicates that deformation at this depth may serve as one of the primary drivers of surface subsidence, especially during high-frequency variations. Furthermore, y-direction (dip direction) deformation at 92 m depth exhibits in-phase correlation with surface subsidence in the low-frequency range but shows a certain degree of lag in the high-frequency range.
(3) The deformation observed at 132 m depth demonstrates complex spatiotemporal characteristics across different frequency bands. In the low-frequency range (periods >16 h), *x*-direction (strike direction) deformation exhibits a negative correlation with surface subsidence and appears to precede surface movement. In the intermediate frequency band (6–16 h), deep deformation lags behind surface displacement, while in the high-frequency range (<6 h), it again leads surface subsidence. These phase relationships suggest that the temporal response of deep horizontal deformation relative to surface vertical displacement varies with timescale, possibly reflecting different interaction dynamics between subsurface and surface processes at each frequency range.

The phase difference results obtained from XWT analysis provide valuable insights into the temporal causality of deformation processes. Specifically, a phase lead of deep deformation relative to surface subsidence suggests that subsurface changes may act as early indicators or precursors of upcoming surface movement. This lead–lag behavior reflects the vertical transmission of mining-induced stress and deformation, where confined or load-bearing strata first respond to stress redistribution before its manifestation at the surface. Conversely, lagging responses at shallow depths may represent delayed mechanical adjustments, influenced by lithological softness or hydrological lag effects. Thus, identifying phase relationships across different depths not only enhances our understanding of stratified deformation dynamics but also holds direct implications for designing early warning systems based on deep-layer precursory signals.

6.2. Temporal correlation characteristics of Multi-Depth Deformation and Surface Subsidence

Deformation behaviors observed at different depths exhibit varying timing and frequency-dependent correlation patterns with surface subsidence. These differences may be associated with variations in lithology, burial depth, and responses to mining-induced disturbances. The following subsections summarize the observed characteristics for each depth level based on time series and cross-wavelet transform analyses.

(1) Response characteristics of the 14 m depth (loess layer). The loose structure and well-developed porosity of the loess layer at this depth make it highly susceptible to precipitation and groundwater level fluctuations (Zhuang et al., 2020). From the time series analysis, deformation at 14 m depth lags behind that at 92 m and 132 m depths, and exhibits a transition from initial compression to later expansion. In cross wavelet transform analysis, deformation at this depth is primarily controlled by surface subsidence in the low-frequency range, while it exhibits a lagging effect in the high-frequency range. These observations may reflect a delayed mechanical response of shallow loess layers, possibly influenced by soil water content variations and structural rearrangement processes as documented in previous loess deformation studies (Cao and Wang, 2022).
(2) Driving role of the 92 m depth (primary subsidence deformation zone). The 92 m depth is primarily composed of interbedded fine sandstone and mudstone, and its deformation characteristics are most strongly correlated with surface subsidence. From the time series analysis, deformation at 92 m depth occurs before the onset of surface subsidence and exhibits synchronous deformation fluctuations during the acceleration phase of subsidence. Cross wavelet transform results show that deformation at this depth exhibits a clear leading effect on surface subsidence in the high-frequency range, indicating that it may be one of the key driving factors for surface subsidence. The 92 m depth rock mass undergoes significant tensile and shear deformation, which may play a critical role in the transmission and acceleration of subsidence.
(3) Observed response characteristics at 132 m depth (Confined Layer). The 132 m depth exhibits the largest horizontal deformation among all monitored layers and is composed mainly of thick-bedded sandstone. According to the time series analysis, x-direction (strike direction) deformation at this depth is detected earlier than in shallower layers. This early signal may reflect that deformation processes at this depth initiate before surface subsidence becomes apparent. In the low-frequency range (>16 hr), cross-wavelet analysis reveals a negative correlation between x-direction (strike direction) deformation and surface subsidence. This phase relationship may indicate asynchronous behavior between the confined layer and the surface during slow deformation phases.

In the intermediate frequency band (6–16 hr), deep deformation lags behind surface displacement, suggesting that surface movement becomes dominant as subsidence accelerates. In contrast, at high frequencies (<6 hr), deep deformation leads to surface subsidence, possibly reflecting localized responses or disturbance signals originating at depth. These frequency-dependent phase patterns highlight the dynamic coupling between surface and deep-layer deformation, with the 132 m layer showing distinctive timing behavior across timescales.

The frequency-dependent phase relationships observed at the 132 m

depth may also reflect internal stress transmission and adjustment processes within the stratified overburden. In particular, the consistent lead of deep deformation in high-frequency bands suggests that this confined layer may act as a stress-absorbing and transmitting medium, capable of responding quickly to mining-induced perturbations. This behavior can be attributed to its high mechanical integrity and burial depth, which allow for the early redistribution of stress before surface manifestations occur. This mechanism is also consistent with basic rock mechanics principles, where deeper strata with greater confining pressure and higher elastic modulus tend to store and redistribute stress over larger areas before yielding, thereby exhibiting broader influence in the early stages of subsidence evolution.

Conversely, the lagging response observed in the intermediate-frequency range indicates that as the subsidence process evolves, the 132 m layer may gradually transition into a passive responder, governed by the deformation behavior of the overlying strata. These contrasting responses across timescales suggest a dynamic shift in the role of this layer—from a trigger during early subsidence initiation to a regulator or adjuster during the coordinated deformation phase. Although direct in situ stress measurements are not available in this study, the consistent phase lead–lag structure offers indirect but valuable clues about subsurface stress propagation paths and timing. Further integration with stress monitoring or seismic data could help clarify these mechanisms.

The observed lead–lag relationships between deep deformation and surface subsidence suggest that internal displacement patterns may serve as early indicators of subsidence evolution, providing valuable inputs for predictive modeling in similar mining environments. In particular, the distinctive time–frequency characteristics of the 132 m confined layer—especially its early activation and dual role in stress buffering and release—indicate that deeper monitoring points can yield more timely and informative signals of evolving deformation.

From an operational perspective, these results highlight the importance of deploying sensors at depths corresponding to mechanically confined or transitional strata. Incorporating deformation signals from such layers into early-warning systems and predictive models may enhance the accuracy and reliability of subsidence forecasting, especially in stratified geological settings where shallow surface responses tend to lag behind stress redistribution at depth. To support practical implementation, we propose preliminary guidelines for how mining operators can apply the results of this study to improve monitoring and prediction strategies:

(1) Deploy deformation sensors at multiple depths, including at confined and transitional strata (e.g., 132 m and 92 m), in addition to surface stations. These layers have demonstrated early deformation responses and can serve as sensitive indicators for subsidence onset.
(2) Adjust early-warning thresholds to incorporate high-frequency deformation signals from deeper layers as precursors. Mining safety systems can benefit from using lead-time deformation signals to trigger earlier alerts.
(3) Incorporate phase-based indicators into predictive models, using the observed lead–lag relationships to inform time-sensitive deformation forecasts. Layer-specific response patterns can be integrated into machine learning or numerical models to enhance prediction resolution.

These measures can help bridge the gap between scientific analysis and operational risk control, improving accuracy, accuracy, and safety in stratified mining environments.

6.3. Applicability and extension of the results to other mining settings

The spatiotemporal characteristics and lead–lag relationships observed between deep deformation and surface subsidence in this study were identified under a specific geological setting, featuring a typical stratified overburden structure. Despite this, the deformation patterns across multiple depths—particularly the early activation of confined layers and the frequency-dependent phase behavior—may be relevant to other mining environments with similar stratigraphy.

The results suggest that subsidence evolution in layered rock masses is not only spatially heterogeneous but also temporally segmented, with deeper layers often initiating movement prior to shallow or surface responses. These observations may inform early-warning designs in other regions by encouraging deep-layer monitoring deployment and emphasizing short-period signal extraction.

However, we recognize that the extent to which these insights can be generalized depends on lithological, hydrological, and mining-related variability. Therefore, further comparative studies across different mining basins are recommended to validate the transferability and operational relevance of the proposed findings.

6.4. Limitations and scope of applicability

While the proposed GNSS–XWT-based deformation analysis framework demonstrates strong interpretability in stratified coal-bearing basins, its broader application must consider several limitations.

First, the studied stratigraphy—loess, interbedded sandstone and mudstone, and thick-bedded sandstone—may not accurately represent hard rock or carbonate settings, where stress transmission and failure mechanisms differ. In such cases, the lead–lag phase characteristics observed here may not reliably serve as precursors.

Second, the method relies on deep borehole installations and continuous surface GNSS monitoring along a vertical plane, which can be challenging to replicate in rugged terrains or areas with drilling and budget constraints. Its effectiveness depends on the availability of high-frequency, co-located monitoring data.

Third, external factors such as rainfall, groundwater variations, or tectonic disturbances may introduce deformation signals that complicate the interpretation of phases. Future applications should integrate hydrological and seismic observations to better discriminate mining-induced deformation.

Fourth, variations in mining methods (e.g., longwall vs. room-and-pillar), panel sizes, and extraction sequences can alter subsurface stress redistribution and deformation timing. Thus, localized calibration and sensitivity testing are necessary when applying the framework to different mining environments.

Despite these limitations, the study offers valuable insights for practical application. The early activation of the 132 m confined sandstone layer highlights the potential of deep deformation signals as early indicators of surface subsidence. Deploying sensors at confined or transitional strata can improve risk detection and enhance early-warning capabilities. Moreover, GNSS–borehole fusion combined with cross-wavelet analysis improves the temporal resolution of subsidence monitoring, enabling earlier detection of deformation transitions.

Our findings are consistent with previous research (Zhuang et al., 2020; Cao and Wang, 2022), which identified delayed responses in shallow loess layers and stress-regulating behavior in deep sandstone units. Building on these insights, this study introduces a synchronized multi-depth monitoring approach coupled with phase-based analysis, offering a dynamic and scalable method for subsidence characterization.

Importantly, the results challenge assumptions in traditional prediction models. The Probability Integral Method (PIM) typically assumes instantaneous surface response to mining, ignoring time-dependent stratified deformation. Finite Element Models (FEM) often rely on fixed parameters and boundary conditions that may not capture frequency-dependent behaviors. The observed lead–lag phase relationships—especially early confined-layer activation and delayed shallow responses—highlight the need to incorporate depth-resolved monitoring and time–frequency coupling into future predictive models to improve accuracy and operational applicability.

7. Conclusion

Based on high-frequency continuous GNSS observations and multi-depth internal deformation monitoring data, this study employed cross wavelet transform analysis to investigate the spatiotemporal evolution characteristics of surface subsidence and rock mass deformation at different depths during mining-induced subsidence. The results show that rock layers at different depths exhibit distinct response patterns and play different roles at various stages of subsidence evolution.

(1) Surface subsidence lags behind deep rock mass deformation, with deep deformation playing a dominant role in the evolution of subsidence. The earliest deformation occurs at 132 m depth, exhibiting a leading effect in short-period variations, indicating that this layer serves as a stress regulation and transmission zone in the early stages of subsidence. The 92 m depth deformation leads to surface subsidence in high-frequency bands, suggesting that it may be a key driving factor of surface subsidence. In contrast, the initiation of surface subsidence lags behind deformation at deeper layers, indicating that subsidence is not merely a surface response, but rather a result of stress adjustment and transmission within deep rock layers.

(2) The deformation patterns of different depth rock layers are controlled by geological properties. The 14 m depth (loess layer) is primarily controlled by surface subsidence, exhibiting a certain degree of lag in high-frequency variations, likely influenced by hydrological conditions and the viscous characteristics of shallow soil layers. The 92 m depth (primary subsidence deformation zone) plays a critical role in subsidence evolution, with high-frequency deformation leading to surface subsidence. In contrast, low-frequency deformation reflects stress adjustments, suggesting that this depth may serve as the primary transmission layer of subsidence. The 132 m depth (confined layer) experiences the largest deformation, exhibiting a leading effect in short periods, but lagging behind surface subsidence in long periods, indicating that it plays a dual role in stress buffering and release during subsidence evolution.

(3) Spatiotemporal characteristics of subsidence evolution. Both deformation time series analysis and cross-wavelet transform results indicate that the acceleration stage of surface subsidence (October 27 – November 16) coincides with synchronous anomalous deformation at all deep layers, reflecting the transition of the subsidence system into a coordinated deformation stage. Additionally, subsidence evolution exhibits significant multi-scale characteristics, where deep deformation can precede surface subsidence over short periods, while long-period subsidence is governed by overall stress redistribution.

Compared with previous studies on mining-induced subsidence, our results reinforce the view that deformation evolves in a stratified and time-dependent manner. While earlier research has primarily focused on surface or near-surface responses, the present time–frequency analysis reveals that deep rock mass deformation can precede surface settlement and exhibit distinct frequency-dependent behaviors. This provides a more nuanced understanding of subsidence evolution and underscores the importance of incorporating multi-depth monitoring and phase-based analysis into future modeling approaches. Furthermore, the observed lead–lag patterns highlight the practical value of multi-depth deformation monitoring for enhancing early-warning systems. By enabling the timely identification of precursory signals, such systems can improve the accuracy of subsidence prediction and contribute to safer underground mining operations.

The insights gained from this study can directly inform the refinement of subsidence prediction models in engineering practice. By revealing the frequency-dependent phase relationships between deep rock mass deformation and surface subsidence, the results emphasize the importance of incorporating multi-depth monitoring into dynamic subsidence modeling frameworks. Specifically, the detection of early deformation signals at confined layers (e.g., 132 m) enables more proactive risk forecasting compared to traditional surface-based methods.

For mining operators, this finding underscores the benefit of deploying deformation meters at strategically selected geological interfaces, thereby capturing stress redistribution trends before they manifest as surface hazards. For policymakers and regulatory agencies, the proposed GNSS–borehole co-monitoring and XWT-based analysis offer a scientifically grounded approach for defining early warning thresholds, supporting zoning of high-risk areas, and improving the timing of safety interventions. As such, the methodology contributes to both predictive accuracy and decision-making efficiency in subsidence management.

CRediT authorship contribution statement

Dongdong Cao: Methodology, Conceptualization. **Jun Zhang:** Data curation. **Ming Li:** Project administration. **Baoqiang Chen:** Formal analysis. **Jia Li:** Investigation. **Xiaolong Wu:** Writing – original draft.

Author agreement and Acknowledgement

All authors agree for this publication. The authors would like to express their sincere appreciation to the editorial board and anonymous reviewers for their constructive comments and valuable suggestions, which have greatly improved the quality of this manuscript.

The authors declare that there are no conflicts of interest regarding this publication.

Declaration of competing interest

The authors declare the following financial interests (e.g., any funding for the research project)/personal relationships (e.g., the author is an employee of a profitable company) which may be considered as potential competing interests: Dongdong Cao, Jun Zhang, Ming Li, Baoqiang Chen and Jia Li are currently employed by China Coal xi 'an Design Engineering co., Ltd. The authors declare that they have no known competing financial interests or personal relationships that could have appeared to influence the work reported in this paper.

References

Bos, M.S., Fernandes, R.M.S., Williams, S.D.P., Bastos, L., 2013. Fast error analysis of continuous GNSS observations with missing data. J. Geod. 87 (4), 351–360. https://doi.org/10.1007/s00190-012-0605-0.

Cao, Y., 2023. Deformation mechanism and stability analysis of coal mining subsidence in soft rock under high-speed railways. Master's thesis Qingdao University of Technology. https://doi.org/10.27263/d.cnki.gqudc.2023.000015.

Cao, Y., Wang, X., 2022. Water-temperature controlled deformation patterns in Heifangtai loess terraces revealed by wavelet analysis of InSAR time series and hydrological parameters. Front. Environ. Sci. 10, 957339.

Chai, H., Xu, H., Hu, J., et al., 2024. Application of a variable weight time function combined model in surface subsidence prediction in goaf area: a case study in China. Appl. Sci. 14 (5), 1748. https://doi.org/10.3390/app14051748.

Chen, D., Chen, H., Zhang, W., et al., 2020a. Characteristics of the residual surface deformation of multiple abandoned mined-out areas based on a field investigation and SBAS-InSAR: a case study in Jilin, China. Remote Sens. 12 (22), 3752.

Chen, B., Li, Z., Yu, C., et al., 2020b. Three-dimensional time-varying large surface displacements in coal exploiting areas revealed through integration of SAR pixel offset measurements and mining subsidence model. Rem. Sens. Environ. 240, 111663.

Chen, B., Yang, Y., Zhang, L., et al., 2024. A novel knowledge-learning coupling method for InSAR phase unwrapping of large surface displacements in coal mining areas. IEEE Trans. Geosci. Rem. Sens. 62, 1–15. https://doi.org/10.1109/TGRS.2024.3492505.

Cun, Y., Yao, B., 2021. Construction of a 3D simulation system for mining subsidence measurement and geology. Surveying and Spatial Geographic Information 44 (11), 165–168.

Diao, X., Sun, Q., Zhang, Y., et al., 2023. Spatiotemporal evolution law and the mechanism of abnormal surface deformation in fault-affected mining zones. IEEE Access 11, 119733–119747. https://doi.org/10.1109/ACCESS.2023.3327255.

Fan, H., Lu, L., Yao, Y., 2018. Method combining probability integration model and a small baseline subset for time series monitoring of mining subsidence. Remote Sens. 10 (9), 1444.
Foufoula-Georgiou, E., Kumar, P., 1995. Wavelets in Geophysics. Academic Press.
Grinsted, A., Moore, J.C., Jevrejeva, S., 2004. Application of the cross wavelet transform and wavelet coherence to geophysical time series. Nonlinear Process Geophys. 11 (5–6), 561–566.
Guo, Y., Luo, L., 2022. Monitoring and analysis of deformation evolution law of fault activation caused by deep mining in Shizishan Copper Mine, China. Appl. Sci. 12 (14), 6863. https://doi.org/10.3390/app12146863.
Jahanmiri, S., Noorian-Bidgoli, M., 2024. Land subsidence prediction in coal mining using machine learning models and optimization techniques. Environ. Sci. Pollut. Control Ser. 31 (22), 31942–31966.
Killick, R., Fearnhead, P., Eckley, I.A., 2012. Optimal detection of changepoints with a linear computational cost. J. Am. Stat. Assoc. 107 (500), 1590–1598. https://doi.org/10.1080/01621459.2012.737745.
Lian, X., Hu, H., 2017. Terrestrial laser scanning monitoring and spatial analysis of ground disaster in Gaoyang coal mine in Shanxi, China: a technical note. Environ. Earth Sci. 76, 1–11.
Miller, M.M., Shirzaei, M., 2015. Spatiotemporal characterization of land subsidence and uplift in Phoenix using InSAR time series and wavelet transforms. J. Geophys. Res. Solid Earth 120 (8), 5822–5842. https://doi.org/10.1002/2015JB012017.
Ministry of Emergency Management, & National Mine Safety Administration, 2022. Notice on Issuing the "14th Five-Year Plan for Mine Safety Production" [S].
Mohebi, B., Yazdanpanah, O., Kazemi, F., et al., 2021. Seismic damage diagnosis in adjacent steel and RC MRFs considering pounding effects through improved wavelet-based damage-sensitive feature. J. Build. Eng. 33, 101847.
Tan, Z., Yang, J., Deng, K., 2021. Research on full-basin mining subsidence parameter estimation method based on SBAS-InSAR. Coal Sci. Technol. 49 (1).
Torrence, C., Compo, G.P., 1998. A practical guide to wavelet analysis. Bull. Am. Meteorol. Soc. 79 (1), 61–78.
Wang, G., Wu, Q., Li, P., et al., 2021a. Mining subsidence prediction parameter inversion by combining GNSS and DInSAR deformation measurements. IEEE Access 9, 89043–89054.
Wang, Z., Li, W., Wang, Q., Hu, Y., Du, J., 2021b. Monitoring the dynamic response of the overlying rock–soil composite structure to underground mining using BOTDR and FBG sensing technologies. Rock Mech. Rock Eng. 54 (11), 5095–5116. https://doi.org/10.1007/s00603-021-02530-y.
Wang, G., Wu, Q., Li, P., Cui, X., Gong, Y., Zhang, J., 2021c. Mining subsidence prediction parameter inversion by combining GNSS and DInSAR deformation measurements. IEEE Access 9, 97822–97835. https://doi.org/10.1109/ACCESS.2021.3089820.
Wang, W., Wu, Z., Wang, P., et al., 2023. Surface dynamic subsidence prediction model and its application based on multi-function crossover. Coal Mine Safety 54 (10), 154–160. https://doi.org/10.13347/j.cnki.mkaq.2023.10.020.
Wang, J., Luo, Z., Zhou, L., et al., 2024. Surface deformation monitoring and subsidence mechanism analysis in Beijing based on time-series InSAR. ISPRS Annals of the Photogrammetry, Remote Sensing and Spatial Information Sciences 10 (1), 233–240. https://doi.org/10.5194/isprs-annals-x-1-2024-233-2024.
Wu, Z., 2021. Geological Disaster Patterns and Disaster Mechanisms in the Mined-Out Collapse Areas of Northern Hebei Mountains [Doctoral Dissertation. China University of Mining and Technology. https://doi.org/10.27623/d.cnki.gzkyu.2021.000071.
Xiao, Y., Tao, Q., Hu, L., et al., 2024. A deep learning-based combination method of spatio-temporal prediction for regional mining surface subsidence. Sci. Rep. 14 (1), 19139.
Yang, X., Yao, Y., Jia, C., et al., 2024. Spatiotemporal prediction of land subsidence and its response patterns to different aquifers in coastal areas. Ocean Coast Manag. 248, 107148. https://doi.org/10.1016/j.ocecoaman.2024.107148.
Yao, W., Gao, K., Zheng, J., et al., 2023. Study on mining subsidence monitoring based on airborne LiDAR point cloud C2C algorithm. Coal Engineering 55 (4), 162–167.
Yazdanpanah, O., Mohebi, B., Kazemi, F., et al., 2022. Development of fragility curves in adjacent steel moment-resisting frames considering pounding effects through improved wavelet-based refined damage-sensitive feature. Mech. Syst. Signal Process. 173, 109038.
Zhang, J., Cheng, Z., 2023. Prediction of surface subsidence of deep foundation pit based on wavelet analysis. Processes 11 (1), 107. https://doi.org/10.3390/pr11010107.
Zhang, K., Hu, H., Lian, X., et al., 2019. Optimization study on the normal time function model for predicting dynamic surface subsidence. Coal Sci. Technol. 47 (9), 235–240. https://doi.org/10.13199/j.cnki.cst.2019.09.030.
Zhang, C., Shi, B., Zhang, S., et al., 2021. Microanchored borehole fiber optics allows strain profiling of the shallow subsurface. Sci. Rep. 11, 1–10. https://doi.org/10.1038/s41598-021-88526-8.
Zhang, Y., Yan, Y., Long, S., et al., 2024a. Mining subsidence dynamic prediction model based on an improved Weibull time function. Rock Soil Mech. 45 (6), 1824–1834. https://doi.org/10.16285/j.rsm.2023.1037.
Zhang, J., Zhang, P., Ji, X., Li, Y., 2024b. Prediction of surface subsidence in Gequan coal mine based on probability integral and numerical simulation. Academic Journal of Engineering and Technology Science. https://doi.org/10.25236/ajets.2024.070102.
Zhuang, Y., Cui, Y., Li, Y., et al., 2020. The structural evolution of undisturbed loess due to water infiltration. Sci. Rep. 10 (1), 13451.